metals

MDPI

Article

A Detailed Analysis of the Microstructural Changes in the Vicinity of a Crack-Initiating Defect in Additively Manufactured AISI 316L

Bastian Blinn [1,*], Jenifer Barrirero [2], Lucía Paula Campo Schneider [2], Christoph Pauly [2], Philipp Lion [1], Frank Mücklich [2] and Tilmann Beck [1]

[1] Institute of Materials Science and Engineering, RPTU Kaiserslautern-Landau, Gottlieb-Daimler Str. 44, 67663 Kaiserslautern, Germany
[2] Functional Materials, Department of Materials Science, Saarland University, Campus D3 3, 66123 Saarbrücken, Germany
* Correspondence: blinn@mv.uni-kl.de

Abstract: The fatigue life of metals manufactured via laser-based powder bed fusion (L-PBF) highly depends on process-induced defects. In this context, not only the size and geometry of the defect, but also the properties and the microstructure of the surrounding material volume must be considered. In the presented work, the microstructural changes in the vicinity of a crack-initiating defect in a fatigue specimen produced via L-PBF and made of AISI 316L were analyzed in detail. Xenon plasma focused ion beam (Xe-FIB) technique, scanning electron microscopy (SEM), and electron backscatter diffraction (EBSD) were used to investigate the phase distribution, local misorientations, and grain structure, including the crystallographic orientations. These analyses revealed a fine grain structure in the vicinity of the defect, which is arranged in accordance with the melt pool geometry. Besides pronounced cyclic plastic deformation, a deformation-induced transformation of the initial austenitic phase into α'-martensite was observed. The plastic deformation as well as the phase transformation were more pronounced near the border between the defect and the surrounding material volume. However, the extent of the plastic deformation and the deformation-induced phase transformation varies locally in this border region. Although a beneficial effect of certain grain orientations on the phase transformation and plastic deformability was observed, the microstructural changes found cannot solely be explained by the respective crystallographic orientation. These changes are assumed to further depend on the inhomogeneous distribution of the multiaxial stresses beneath the defect as well as the grain morphology.

Keywords: deformation-induced austenite-α'-martensite transformation; laser-based powder bed fusion (L-PBF); scanning electron microscopy (SEM); electron backscattered diffraction (EBSD); plastic deformation; high cycle fatigue; lack of fusion

Citation: Blinn, B.; Barrirero, J.; Campo Schneider, L.P.; Pauly, C.; Lion, P.; Mücklich, F.; Beck, T. A Detailed Analysis of the Microstructural Changes in the Vicinity of a Crack-Initiating Defect in Additively Manufactured AISI 316L. *Metals* **2023**, *13*, 342. https://doi.org/10.3390/met13020342

Academic Editor: Giovanni Meneghetti

Received: 4 January 2023
Revised: 2 February 2023
Accepted: 3 February 2023
Published: 8 February 2023

1. Introduction

Additive manufacturing (AM) has a high potential to improve the performance of highly loaded components because of an enormous degree of freedom in design, far beyond the possibilities of conventional manufacturing techniques. Besides the new possibilities regarding the geometry of the component, AM also offers the potential to vary the microstructure, and thus the mechanical properties, locally. To exploit the high and diverse potentials of AM, a sound knowledge of the additively manufactured microstructure and its relation to the manufacturing process as well as the resulting mechanical properties is a prerequisite.

Because of the relatively high precision achievable with laser-based powder bed fusion (L-PBF), it is one of the most frequently used AM techniques. Because of the small melt pool sizes, this AM process results in very high solidification rates. From the literature,

it is well known that the grains in the austenitic stainless CrNi steel AISI 316L produced via L-PBF are elongated along the building direction because of the directed heat flux into the already solidified material [1–4]. Moreover, the melt pool boundaries are visible in the microstructure [1,4–6]. Although the grain growth is dedicated to the melt pool geometry [4,7], the grains grow beyond the melt pool boundaries [1,8,9], which is caused by partial melting of the already solidified grains in the previously produced layer. As a result of the high solidification rates, Liu et al. [5] report a dendritic microstructure in AISI 316L with a specific cell structure of dislocations combined with segregation of alloying elements. Furthermore, a variation in the process parameters can lead to a textured microstructure of AISI 316L, which significantly influences the deformation behavior [10]. Consequently, the microstructure can be modified locally by changing the process parameters.

Besides the specific grain structure, additively manufactured metals contain a high number of process-induced defects [2,8,11–13]. For L-PBF, spherical gas pores as well as irregularly shaped defects, which are caused by an incomplete binding and are defined as lack of fusion (LOF) [11,12], can be observed. As LOF defects result from an insufficient binding between different melt pools, this type of defect is located at the melt pool boundaries [11,14].

Compared with the monotonic properties of additively manufactured AISI 316L, which is well described in literature [2,3,5,8,15], the fatigue behavior was analyzed to a lesser extent. However, the works available from other researchers [16–18] and our previous work [19–21] on AISI 316L show that the process-induced defects act as microstructural notches leading to crack initiation under cyclic loading. While the monotonic strength of the AISI 316L manufactured via L-PBF is similar or even higher in relation to conventionally manufactured material [3,5,8,15], the fatigue strength is smaller owing to the process-induced defects [8,13,15]. During cyclic loading, crack initiation starts at the most critical defect in the material volume, and thus not the overall porosity, but the maximum defect size is most relevant for an evaluation of the fatigue life [22]. In this context, Stern et al. [11] demonstrate that the LOF defects in AISI 316L are very critical, owing to the pronounced stress concentrations occurring at their sharp edges, which is in accordance with Sanaei et al. [14]. Thus, the fatigue life of AISI 316L manufactured via L-PBF strongly depends on process-induced defects, hence their influence must be analyzed thoroughly.

Besides the size and the geometry of the defect, the sensitivity of the material to the microstructural notch effect, i.e., the defect tolerance, needs to be considered. As shown by Leuders et al. [13] on specimens produced via L-PBF, AISI 316L yields a less pronounced defect-induced decrease in fatigue strength compared with Ti6Al4V, which can be explained by the higher ductility of the stainless steel, corresponding to a higher defect tolerance. This correlates to our own work [19–21] on additively manufactured AISI 316L, which showed that an increased defect tolerance significantly improves the fatigue strength. As the damage mechanisms occur locally at the crack initiation sites, the microstructure in the vicinity of the initiated fatigue crack, and thus near the defect, strongly influences the crack propagation, which was demonstrated by Brenne et al. [10] in crack propagation analyses. Moreover, in our own work [19] on AISI 316L, a deformation-induced phase transformation from austenite into α'-martensite increased the defect tolerance. This is in accordance with the research of Grigorescu et al. [23] on conventionally manufactured AISI 316L, who showed that local transformations from austenite to α'-martensite in the vicinity of the crack tip decelerate the crack growth, and thus increase the fatigue life. Consequently, the local effects of austenite–α'-martensite transformation are highly relevant for the fatigue behavior of AISI 316L manufactured via L-PBF.

In conclusion, process-induced defects have a strong influence on the fatigue life of additively manufactured AISI 316L, which depends on the defect tolerance of the material volume. However, in most available works, solely the shape and size of the defects are considered, while the defect tolerance, which depends on the local microstructure in the defect's vicinity as well as the respective microstructural changes during fatigue loading, is neglected. For AISI 316L, also the effects of deformation-induced phase transformation are

mostly not considered sufficiently. Consequently, in this work, the local microstructure in the vicinity of a crack-initiating defect of a cyclically loaded and fractured specimen made of AISI 316L, which was produced via L-PBF, was analyzed, focusing specifically on the deformation-induced phase transformation.

2. Materials and Methods

2.1. Material

To examine the fatigue-induced microstructural changes, the microstructure in the vicinity of a crack-initiating defect was analyzed. For this, microstructural analyses beneath the crack initiation site of one specimen fractured at N_f = 426,061 after uniaxial cyclic loading at a stress amplitude of σ_a = 360 MPa were performed. The corresponding fatigue test was performed on a servo-hydraulic testing device of the type Schenck PSA 40 kN with a frequency of f = 2 Hz at a stress ratio of $R = -1$.

The specimen investigated is made of the austenitic stainless CrNi steel AISI 316L and was manufactured via L-PBF with a 3D Systems ProX DMP 320 device (3DSystems GmbH, Rock Hill, SC, USA), using a laser power of 250 W, a scan velocity of 900 mm/s, a hatching distance of 100 µm, and a layer thickness of 30 µm. For the L-PBF process, a 500 W fiber laser with a wavelength of 1070 nm and an atmosphere of nitrogen for oxidation prevention were utilized. Within a single layer, firstly the inner material and then the contour were scanned, while the scanning direction was rotated from layer to layer by an angle of 245°. Using these process parameters, a cylindrical bar with a diameter of 14 mm and a length of 122 mm was produced and subsequently turned to the final geometry of the fatigue specimen given in Figure 1, which is in accordance with DIN 50100 [24].

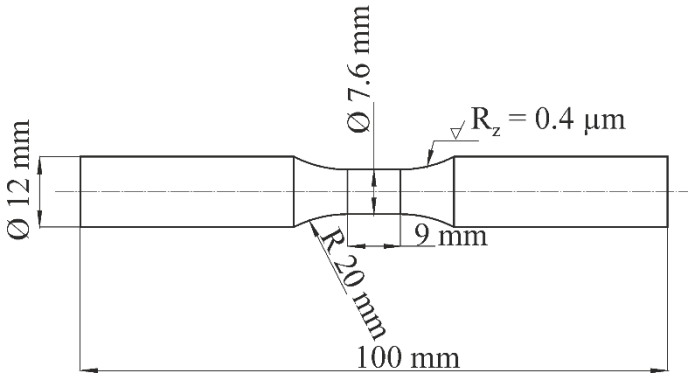

Figure 1. Geometry of the fatigue specimen.

Note that the specimen used for the detailed microstructural analyses in this work is content of a previously published work [20], where detailed information about the influence of a heat treatment and the orientation of the loading direction relative to the building direction on the fatigue behavior is discussed. In this previous work, two different orientations of the layer planes relative to the loading direction, i.e., parallel and perpendicular, were investigated in the "as-built" as well as in a heat-treated condition. To reduce the process-induced residual stresses, a stress-relief heat treatment (650 °C, 2 h; furnace cooling) was performed on the specimens still placed on the built plate. Thus, the "as-built" specimens were manufactured at a separate built plate. For each of these conditions, at least nine fatigue tests were performed to determine representative Woehler curves. These investigations revealed a strong influence of process-induced defects as well as the defect tolerance of the material volume on the fatigue life. Thus, one specimen being representative for defect-induced fracture was selected for the microstructural analyses presented in this work. The specimen investigated here was manufactured vertically, leading to layer planes oriented perpendicular to the loading direction (see Figure 2), and received a stress-relief heat treatment.

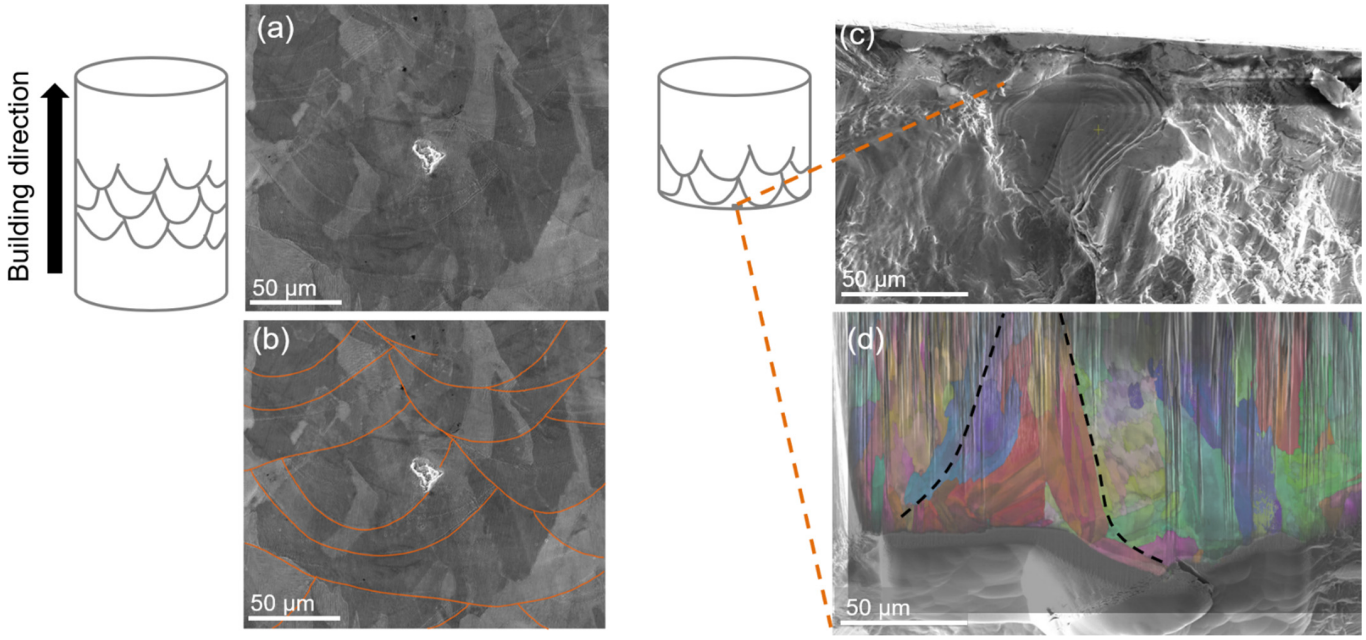

Figure 2. (**a**,**b**) Example of a lack of fusion (LOF) defect in the volume of the material and (**c**) the crack-initiating defect observed in the specimen investigated (top view) as well as (**d**) the microstructure in the vicinity of this defect (cross-sectional view; EBSD IPF map overlay on SEM image; facture surface at the bottom).

As demonstrated in [19,20], a deformation-induced transformation of austenite into α'-martensite significantly influences the fatigue behavior of additively manufactured AISI 316L. Consequently, the austenite stability must be considered for a comprehensive microstructural analysis. Therefore, M_{d30}, which is defined as the temperature that leads to a transformation of 50% of the initial austenitic phase into α'-martensite at a plastic deformation of 30%, was determined in °C according to Angel [25] with Equation (1).

$$M_{d30,Angel} = 413 - 462(C + N) - 9.2Si - 8.1Mn - 13.7Cr - 9.5Ni - 18.5Mo \quad (1)$$

For this, the chemical composition of the material in wt.% is required, which was determined by spectrophotometry and is given in Table 1. The $M_{d30,Angel}$ determined for the specimen is relatively low compared with the limits defined by the ASTM standard [26]. Moreover, for conventionally manufactured AISI 316L, a $M_{d30,Angel}$ = 9.1 °C was obtained in [27], which is significantly higher than the $M_{d30,Angel}$ of the specimen investigated here. As low $M_{d30,Angel}$ indicates a high austenite stability, a relatively high phase stability can be assumed for the material investigated in the presented work.

Table 1. Chemical composition in wt.% and resulting $M_{d30,Angel}$ in °C of the specimen investigated as well as the limits defined in the ASTM standard [26].

	C	N	Si	Mn	Cr	Ni	Mo	Fe	$M_{d30,\ Angel}$
specimen	0.02	0.06	0.40	0.36	17.71	12.97	2.47	bal.	−41.7
ASTM min.	-	-	-	-	16.00	10.00	2.00	bal.	61.8
ASTM max.	0.03	0.10	1.00	2.00	18.00	15.00	3.00	bal.	−117.1

2.2. Methods

The crack-initiating defect was found near the surface of the cylindrical specimen (see Figure 3a). A cross-section across the defect and parallel to the building direction was prepared by a Xenon plasma FIB/SEM (Helios G4 PFIB CXe, Thermo Fisher Scientific, The

Netherlands). To avoid curtaining artifacts and damaging of the specimen surface, a protective layer of Pt-C was deposited by ion beam-induced deposition on a 160 µm × 90 µm surface, covering the defect and the surrounding area. Triangular regions (200 µm wide) at both sides of the region of interest (ROI) were ion-milled (2.5 µA; 30 kV) to avoid a shadowing effect during the EBSD measurement (see Figure 3a). The ion-polishing of the ROI was performed with 200 µm wide and 60 µm deep cleaning cross-section patterns at an acceleration voltage of 30 kV and decreasing currents (1 µA, 0.5 µA, and 0.2 µA).

After the Xe-FIB cut, the EBSD measurements were performed without breaking the vacuum using an EDAX Velocity Plus camera and the software APEX EBSD 2.0. Therefore, the electron beam was accelerated with 20 kV and 26 nA. The respective scans were performed with a step size of 100 nm and a camera binning of 4 × 4 on a hexagonal grid.

For the post-processing and the evaluation of the data obtained by EBSD, the EDAX OIM Analysis 8.6 software was utilized. Thereby, a grain confidence index standardization with 5° of tolerance and 2 pixels minimum grain size followed by a grain dilation (single iteration) were used. Note that pixels with a confidence index below 0.09 were filtered out.

For a detailed analysis of the deformation-induced phase transformation, a reconstruction of the austinite grains (parent phase) from the α'-martensite grains (child phase) was performed, using the orientation relationship according to Kurdjumov–Sachs, which is imbedded in the EDAX OIM Analysis 8.6 software. As a basis for the analysis of the distribution of the Young's modulus *E*, the reconstructed microstructure was visualized according to [28], using MTEX, a free Matlab toolbox.

3. Results and Discussion

In Figure 2a, an example of an LOF defect caused by an insufficient binding of two adjacent melt pools is shown. Figure 2b highlights the location of this process-induced defect directly at the melt pool boundary, which is marked in orange. At the fracture surface of the specimen investigated in this work (see Figure 2c), an LOF defect can also be observed. Using the Xe-FIB technique, a plane perpendicular to the fracture surface and across the defect was prepared to enable the analysis of the microstructure beneath and in the vicinity of the crack-initiating defect (see Figure 2d). The EBSD measurements show a grain elongation parallel to the building direction and a grain structure arranged in accordance with the melt pool geometry. Considering the LOF defect shown in Figure 2a,b, the microstructure observed in Figure 2d indicates that the defect shown in Figure 2c is also located at the melt pool boundary.

To analyze the microstructure in the vicinity of the crack-initiating LOF defect, the cyclic loading applied on the specimen, and thus fatigue-induced changes in the microstructure, must be considered. For a detailed characterization of the microstructure, EBSD analyses at two different planes across the defect and distanced by approximately 10 µm (see Figure 3b,c) were conducted. Based on the EBSD measurements, the grain structure (see Figure 3d,e) and the distribution of austenite and α'-martensite (see Figure 3f,g) in the vicinity of the defect were determined.

Note that, in the analyses illustrated in Figure 3, the fracture surface is shown with an orientation of the building direction from the top to the bottom, while in Figure 2b, the building direction is oriented from the bottom to the top. This 180° rotation of the orientation of the micrographs was used for an easier visualization of the microstructure beneath the defect.

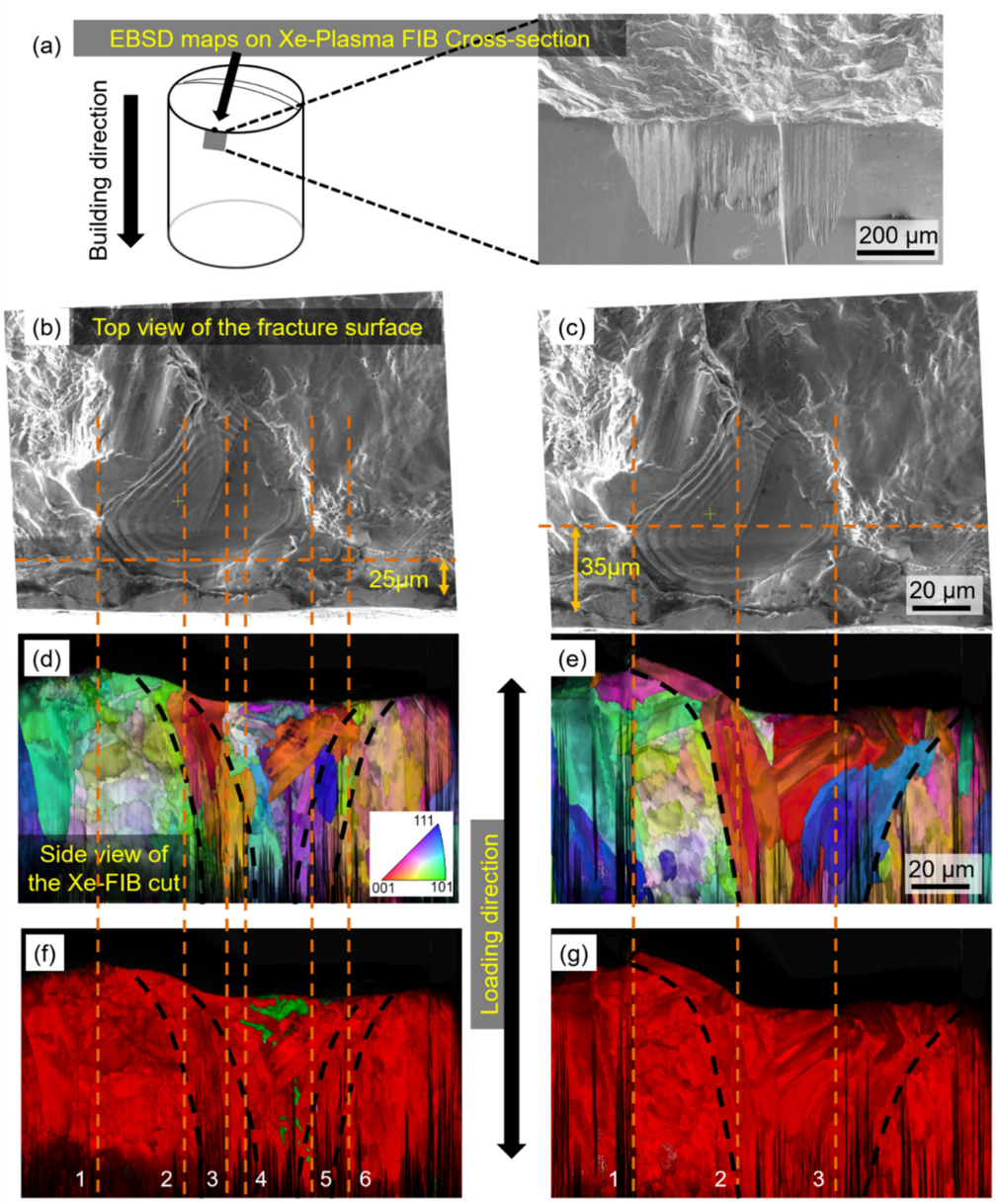

Figure 3. (**a**) Schematic of the PFIB cross section with an SEM image of the region prepared for EBSD. (**b**,**c**) Top view SEM images of the fracture surface including the LOF defect. The orange horizontal lines show the position of the cross section. (**d**,**e**) Inverse pole figure (color) combined with image quality (grey level) maps showing the grain structure. (**f**,**g**) Phase maps (color) combined with image quality (grey level) maps showing austenite (red) and α′-martensite (green) in the vicinity of the crack initiation site. Note that (**d**–**g**) show cross-sectional views with the crack surface perpendicular at the upper edge of the image. The lines 1 to 6 indicate the location of the microstructure in the cross-sectional views in relation to the fracture surface.

Both cross sections reveal a grain elongation parallel to the building direction and an arrangement of the grains according to the melt pool geometry (see Figure 3d,e). In accordance with our own work related to this study [20], α′-martensite can be observed in the vicinity of the crack-initiating defect. As expected, the average grain size of the α′-martensite (equivalent diameter d_e = 3.05 ± 2.51 µm) is smaller in relation to the austenite (d_e = 5.21 ± 3.43 µm), because the α′-martensite evolves from the austenite grains. Note that, in the previous work, Feritscope™ (Helmut Fischer GmbH, Germany) measurements were performed to determine the ferromagnetic fraction in the gauge length of the specimens. As the austenite is paramagnetic and the α′-martensite is ferromagnetic,

this enabled to determine the extent of the phase transformation caused by cyclic loading. As shown by the Ferritcope^{TM} measurements and EBSD analyses performed in previous work [20], the material is fully austenitic in the initial state. After fatigue loading, the specimen presented in this work revealed 0.39 Fe-% ferromagnetic phase, which indicates a relatively small amount of phase transformation. As demonstrated by EBSD analyses performed in [20] at another specimen, these small amounts of phase transformations are not homogeneously distributed in the material volume, but locally at microstructural inhomogeneities, e.g., process-induced defects. Consequently, the α'-martensite observed in Figure 3f,g results from deformation-induced phase transformation caused by cyclic loading.

However, the phase transformation does not occur homogeneously in the material volume around the LOF defect. In Figure 3f, only the region between lines 3 and 6 exhibits a phase transformation, which is also strongly localized and most pronounced in the region between the lines 4 and 5. Note that these regions are not directly beneath the defect, but in the surrounding region in direct contact with it. According to Murakami [29], the crack initiation at a defect takes place immediately at the beginning or at least in an early phase of the fatigue test, hence the border region between the defect and the surrounding material volume is located in the plastic zone in front of the crack tip, receiving high stress concentrations during cyclic loading. It should be noted that the propagation of this short crack takes the main part of the fatigue life, and thus the regions in direct contact with the defect receive the highest amount of accumulated cyclic plastic strain. In correspondence with this, Grigorescu et al. [23] showed that a short crack propagation results in a localized deformation-induced phase transformation. This phase transformation is accompanied by a volume expansion of the lattice, leading to compressive residual stresses, which decelerates the crack propagation rate and increases the fatigue life. Comparing the results shown in Figure 3f with the phase distributions observed at the Xe-FIB cut 10 µm deeper in the specimen (see Figure 3g), substantial differences can be seen. Although the region imaged in Figure 3g is in direct contact with the defect, which results in locally increased stresses, no pronounced phase transformation is present. It can be then deduced that not only the stress concentration caused by the notch effect, but also the amount of accumulated plastic strain of the grains as well as their phase stability, are relevant for the phase transformation. In this context, it must be considered that both the amount of plastic deformation and the austenite stability depend on the local crystallographic orientation, which is discussed in the following.

Figure 4 shows a more detailed view of the region around the defect. In the image quality maps of Figure 4e,f, slip bands can be seen in the vicinity of the crack initiation site. In addition, kernel average misorientation (KAM) maps, which are given in Figure 4g,h, show that a higher level of local misorientations, generally related to higher dislocation densities, and thus more pronounced plastic deformation, is observed in the regions that showed phase transformation and slip band formation. These regions are directly located at the edge of the defect, thus it can be assumed that they receive strong stress concentrations and a high accumulated cyclic plastic strain. Note that, for some grains, the accumulated cyclic plastic deformation led to austenite-α'-martensite transformation, while other grains only show an austenitic phase and the formation of slip bands. This evidence may be related to a difference in the behavior of the microstructure according to the crystallographic orientations of the grains surrounding the defect.

To analyze the influence of the grain orientation on the phase transformation and plastic deformation caused by cyclic loading, a parent grain reconstruction was performed from the α'-martensite (child phase) to the austenite (parent phase). The resulting EBSD data were analyzed and the grain structure was visualized according to [28], which is shown in Figure 5a. Moreover, Figure 5b illustrates the grains that transformed into α' martensite. In correspondence with [30] and based on the data reported by Teklu et al. [31] for an austenitic steel with 18 wt.% Cr and 12 wt.% Ni, the Young's modulus E in the loading

direction of the fatigue tests was calculated for each grain of this parent microstructure. Therefore, the Euler angles obtained from the EBSD measurements were used.

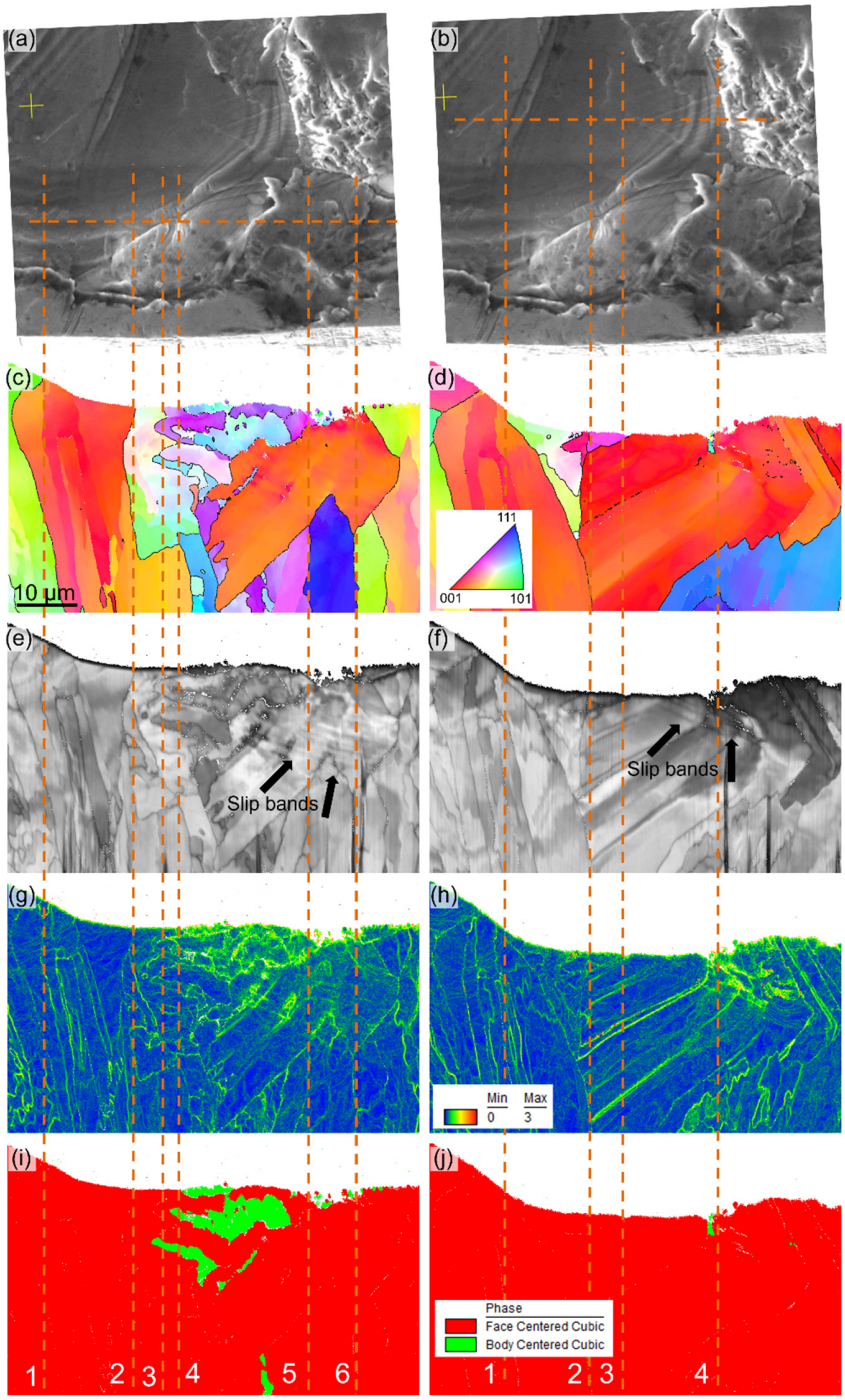

Figure 4. (**a**,**b**) SEM top view images of the LOF defect and its surrounding microstructure (orange horizontal lines show the position of the cross section). (**c**,**d**) Inverse pole figure maps showing the grain structure. (**e**,**f**) Image quality maps showing intragrain orientation gradients and slip bands. (**g**,**h**) Kernel average misorientation maps showing local deformation and subgrain boundaries. (**i**,**j**) Phase maps showing austenite (red) and α'-martensite (green). Note that (**c**–**j**) show cross-sectional views with the crack surface located perpendicular at the upper edge of the images. The lines 1 to 6 indicate the location of the microstructure in the cross-sectional views in relation to the fracture surface.

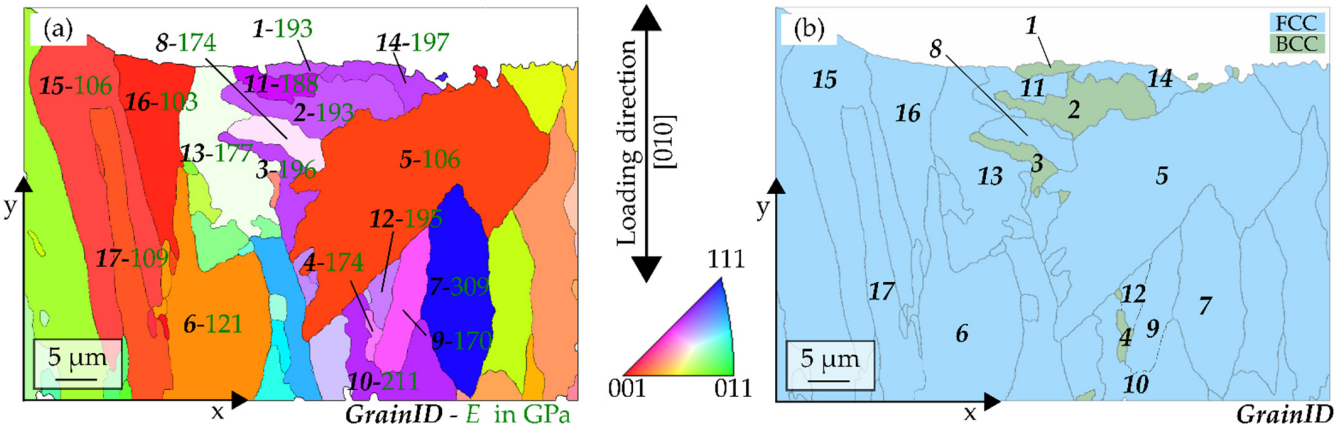

Figure 5. Illustration of the calculated initial austenitic microstructure (parent microstructure) including the information of the Young's modulus *E* in GPa of selected grains (**a**) and the corresponding microstructure calculation, showing the deformation-induced phase transformation (**b**).

As can be seen from Figure 5b, only the grains with ID 1 to 4 yield a deformation-induced phase transformation. These grains are oriented roughly similar, i.e., with the [−1 6 10] direction parallel to the building and loading direction (see Figure 5a). However, some grains also oriented roughly in the same direction did not transform to α'-martensite (grains with the ID 9 to 12 and 14). Consequently, it can be assumed that this orientation encourages the phase transformation, but also requires a sufficiently high cyclic plastic deformation. As the stress distribution beneath the defect is inhomogeneous, it is expected that the grains that did not transform to α'-martensite did not receive sufficient stresses, and thus cyclic plastic deformation.

In this context, it must be noted that, in austenitic CrNi steels, the Young's modulus also depends on the crystallographic orientation with respect to the loading direction. Thus, the grain orientation around the defect affects the distribution of the stress and strain in this area. When analyzing the calculated Young's modulus of the different grains (see Figure 5a), it must be considered that the crack-initiating defect results in multiaxial stresses [32] and thus deviates from the uniaxial stress that could be expected in the case of a fully dense volume under the given loading. However, despite the multiaxial stress state, the maximum tensile stress will occur parallel to the loading direction in the fatigue test, thus the calculated *E* can be used for a qualitative analysis.

From the calculated *E*, relatively large differences in elastic stiffness are obtained, increasing the inhomogeneity in the stress distribution. As the grains observed are relatively small, a high influence of the contiguous grains on the plastic deformation, and thus phase transformation, is expected. Considering the grain with ID5, the KAM in Figure 4g and the slip band formation shown in Figure 4e indicate pronounced cyclic plastic deformation. This means, that the grain achieved a high level of accumulated cyclic plastic strain, which however, did not lead to a deformation-induced transformation from austenite into α'-martensite. Thus, it can be assumed that the orientation is crucial for the occurrence of phase transformation. However, other factors influencing the deformation must also be considered, such as the orientation, size, and morphology of the surrounding grains as well as the stress distribution caused by the defect. The grains with ID 15 to 17 are oriented roughly in accordance with the grain with ID 5, but they reveal no pronounced cyclic plastic deformation, which underlines that the level of plastic strain yield in the single grains also depends on the orientation of the contiguous grains as well as the stresses induced by the notch effect resulting from the defect.

The presented results indicate that certain grain orientations are beneficial for a plastic deformation (e.g., ID 1 to 5, 10, 11, and 14) and a deformation-induced transformation from austenite into α'-martensite (e.g., ID 1 to 4), and thus can lead to a higher defect tolerance when occurring in the vicinity of a process-induced defect. Some orientations result in a

strong cyclic plastic strain without phase transformation (e.g., ID 5), which, however, also increases the defect tolerance because the stress intensities at the defects are translated into cyclic plastic deformation instead of crack propagation. Owing to the high solidification rate of AM processes, and because the LOF defects are often formed at the end of the solidification of liquid trapped between solidifying melting pools, defects are surrounded by relatively fine grains. Consequently, the probability of grains being beneficially oriented for slip band formation and phase transformation is relatively high, which both lead to synergistic effects for a deceleration in the fatigue crack propagation.

4. Summary and Conclusions

In the presented work, the microstructure in the vicinity of the crack-initiating defect of a fractured fatigue specimen (N_f = 426,061; σ_a = 360 MPa; $R = -1$; f = 2 Hz) manufactured via L-PBF and made of the austenitic stainless CrNi steel AISI 316L was analyzed in detail. Thereby, the local plasticization and deformation-induced phase transformation caused by the cyclic loading was focused. From the results presented, the following conclusions can be drawn:

- The grain structure beneath the process-induced lack of fusion defect is arranged in accordance with the melt pool geometry. Moreover, a relatively fine grain structure was obtained in the vicinity of the defect, which is caused by the high solidification rates resulting from the L-PBF process.
- As shown by kernel average misorientation maps, the cyclic loading results in a pronounced plastic deformation in the vicinity of the crack initiating defect, being most pronounced at the border region between the defect and the surrounding material volume. As the defect can be interpreted as equivalent to a crack [29], this region exhibits relatively high stress intensities for a high number of cycles, leading to a strong accumulated cyclic plastic deformation during short crack propagation.
- The more pronounced cyclic plastic deformation at the border region results in a substantial deformation-induced transformation of the austenite into α'-martensite, which increases the defect tolerance, and thus the fatigue life.
- The plastic deformation and phase transformation vary locally in the vicinity of the defect and are influenced by the crystallographic orientations of the grains. In this context, the presented results indicate that certain grain orientations are beneficial for deformation-induced phase transformation, while other specific orientations tend to deform plastically. However, the orientation solely cannot explain the local differences observed, thus the surrounding grain morphology as well as the inhomogeneous distribution of the multiaxial stresses around the defect are assumed to influence the microstructural changes. To verify these assumptions, a thorough analysis and a broader data basis, such as that obtained by a 3D-EBSD dataset, would be of advantage.

As local phase transformation and cyclic plasticization increase the defect tolerance and decelerate the crack propagation, which results in a higher fatigue life, it is of scientific interest to analyze in detail what kind of microstructure encourages a deformation-induced austenite-α'-martensite transformation and a local plasticization. Moreover, it is of great interest how these effects can be intensified by a variation in the additive manufacturing process. Therefore, further microstructural analyses of crack-initiating defects of additively manufactured AISI 316L are required.

Author Contributions: Conceptualization, J.B. and B.B.; methodology, J.B., L.P.C.S., C.P. and P.L.; investigation, J.B., L.P.C.S., C.P. and P.L.; resources, T.B. and F.M.; writing—original draft preparation, J.B. and B.B.; writing—review and editing, J.B., B.B., L.P.C.S., C.P., P.L., T.B. and F.M.; visualization, J.B. and P.L.; supervision, T.B. and F.M.; project administration, J.B. and B.B.; funding acquisition, T.B. and F.M. All authors have read and agreed to the published version of the manuscript.

Funding: The PFIB/SEM instrument at Saarland University was funded by DFG (INST 256/510-1 FUGG).

Data Availability Statement: Not applicable.

Acknowledgments: Besides the finical support of the funders, the support of the colleagues of the Institute for Mechanical and Automotive Design of RPTU Kaiserslautern-Landau, namely R. Teutsch and M. Ley, is thankfully acknowledged. We also acknowledge the priority research activity of Rhineland Palatinate "Ad-vanced Materials Engineering (AME)".

Conflicts of Interest: The authors declare no conflict of interest. The funders had no role in the design of the study; in the collection, analyses, or interpretation of data; in the writing of the manuscript; or in the decision to publish the results.

References

1. Yasa, E.; Kruth, J.-P. Microstructural investigation of Selective Laser Melting 316L stainless steel parts exposed to laser re-melting. *Procedia Eng.* **2011**, *19*, 389–395. [CrossRef]
2. Lewandowski, J.J.; Seifi, M. Metal Additive Manufacturing: A Review of Mechanical Properties: A Review of Mechanical Properties. *Annu. Rev. Mater. Res.* **2016**, *46*, 151–186. [CrossRef]
3. Riemer, A.; Leuders, S.; Thöne, M.; Richard, H.A.; Tröster, T.; Niendorf, T. On the fatigue crack growth behavior in 316L stainless steel manufactured by selective laser melting. *Eng. Fract. Mech.* **2014**, *120*, 15–25. [CrossRef]
4. Casati, R.; Lemke, J.; Vedani, M. Microstructure and Fracture Behavior of 316L Austenitic Stainless Steel Produced by Selective Laser Melting. *J. Mater. Sci. Technol.* **2016**, *32*, 738–744. [CrossRef]
5. Zhong, Y.; Liu, L.; Wikman, S.; Cui, D.; Shen, Z. Intragranular cellular segregation network structure strengthening 316L stainless steel prepared by selective laser melting. *J. Nucl. Mater.* **2016**, *470*, 170–178. [CrossRef]
6. Liu, L.; Ding, Q.; Zhong, Y.; Zou, J.; Wu, J.; Chiu, Y.-L.; Li, J.; Zhang, Z.; Yu, Q.; Shen, Z. Dislocation network in additive manufactured steel breaks strength–ductility trade-off. *Mater. Today* **2018**, *21*, 354–361. [CrossRef]
7. Wang, Y.M.; Voisin, T.; McKeown, J.T.; Ye, J.; Calta, N.P.; Li, Z.; Zeng, Z.; Zhang, Y.; Chen, W.; Roehling, T.T.; et al. Additively manufactured hierarchical stainless steels with high strength and ductility. *Nat. Mater.* **2018**, *17*, 63–71. [CrossRef]
8. Mower, T.M.; Long, M.J. Mechanical behavior of additive manufactured, powder-bed laser-fused materials. *Mater. Sci. Eng. A* **2016**, *651*, 198–213. [CrossRef]
9. Yu, J.; Rombouts, M.; Maes, G. Cracking behavior and mechanical properties of austenitic stainless steel parts produced by laser metal deposition. *Mater. Des.* **2013**, *45*, 228–235. [CrossRef]
10. Brenne, F.; Niendorf, T. Damage tolerant design by microstructural gradation—Influence of processing parameters and build orientation on crack growth within additively processed 316L. *Mater. Sci. Eng. A* **2019**, *764*, 138186. [CrossRef]
11. Stern, F.; Tenkamp, J.; Walther, F. Non-destructive characterization of process-induced defects and their effect on the fatigue behavior of austenitic steel 316L made by laser-powder bed fusion. *Prog. Addit. Manuf.* **2020**, *5*, 287–294. [CrossRef]
12. Sanaei, N.; Fatemi, A.; Phan, N. Defect characteristics and analysis of their variability in metal L-PBF additive manufacturing. *Mater. Des.* **2019**, *182*, 108091. [CrossRef]
13. Leuders, S.; Lieneke, T.; Lammers, S.; Tröster, T.; Niendorf, T. On the fatigue properties of metals manufactured by selective laser melting—The role of ductility. *J. Mater. Res.* **2014**, *29*, 1911–1919. [CrossRef]
14. Sanaei, N.; Fatemi, A. Defects in additive manufactured metals and their effect on fatigue performance: A state-of-the-art review. *Prog. Mater. Sci.* **2021**, *117*, 100724. [CrossRef]
15. Spierings, A.; Starr, T.; Wegener, K. Fatigue performance of additive manufactured metallic parts. *Rapid Prototyp. J.* **2013**, *19*, 88–94. [CrossRef]
16. Günther, J.; Krewerth, D.; Lippmann, T.; Leuders, S.; Tröster, T.; Weidner, A.; Biermann, H.; Niendorf, T. Fatigue life of additively manufactured Ti–6Al–4V in the very high cycle fatigue regime. *Int. J. Fatigue* **2017**, *94*, 236–245. [CrossRef]
17. Beretta, S.; Romano, S. A comparison of fatigue strength sensitivity to defects for materials manufactured by AM or traditional processes. *Int. J. Fatigue* **2017**, *94*, 178–191. [CrossRef]
18. Masuo, H.; Tanaka, Y.; Morokoshi, S.; Yagura, H.; Uchida, T.; Yamamoto, Y.; Murakami, Y. Influence of defects, surface roughness and HIP on the fatigue strength of Ti-6Al-4V manufactured by additive manufacturing. *Int. J. Fatigue* **2018**, *117*, 163–179. [CrossRef]
19. Blinn, B.; Krebs, F.; Ley, M.; Gläßner, C.; Smaga, M.; Aurich, J.C.; Teutsch, R.; Beck, T. Influence of the Chemical Composition of the Used Powder on the Fatigue Behavior of Additively Manufactured Materials. *Metals* **2019**, *9*, 1285. [CrossRef]
20. Blinn, B.; Krebs, F.; Ley, M.; Teutsch, R.; Beck, T. Determination of the influence of a stress-relief heat treatment and additively manufactured surface on the fatigue behavior of selectively laser melted AISI 316L by using efficient short-time procedures. *Int. J. Fatigue* **2020**, *131*, 105301. [CrossRef]
21. Blinn, B.; Ley, M.; Buschhorn, N.; Teutsch, R.; Beck, T. Investigation of the anisotropic fatigue behavior of additively manufactured structures made of AISI 316L with short-time procedures PhyBaLLIT and PhyBaLCHT. *Int. J. Fatigue* **2019**, *124*, 389–399. [CrossRef]
22. Romano, S.; Brückner-Foit, A.; Brandão, A.; Gumpinger, J.; Ghidini, T.; Beretta, S. Fatigue properties of AlSi10Mg obtained by additive manufacturing: Defect-based modelling and prediction of fatigue strength. *Eng. Fract. Mech.* **2018**, *187*, 165–189. [CrossRef]
23. Grigorescu, A.; Hilgendorff, P.-M.; Zimmermann, M.; Fritzen, C.-P.; Christ, H.-J. Cyclic deformation behavior of austenitic Cr–Ni-steels in the VHCF regime: Part I—Experimental study. *Int. J. Fatigue* **2016**, *93*, 250–260. [CrossRef]

24. Deutsches Institut für Normung. *DIN 50100: Load Controlled Fatigue Testing—Execution and Evaluation of Cyclic Tests at Constant Load Amplitudes on Metallic Specimens and Components*; Beuth Verlag GmbH: Berlin, Germany, 2016.
25. Angel, T. Formation of martensite in austenitic stainless steel—Effects of deformation, temperature and composition. *J. Iron Steel Inst.* **1954**, *177*, 165–174.
26. ASTN A182/A182M-22. Standard Specification for Forged or Rolled Alloy and Stainless Steel Pipe Flanges, Forged Fittings, and Valves and Parts for High-Temperature Service. ASTM International: West Conshohocken, PA, USA, 2022.
27. Blinn, B.; Klein, M.; Gläßner, C.; Smaga, M.; Aurich, J.; Beck, T. An Investigation of the Microstructure and Fatigue Behavior of Additively Manufactured AISI 316L Stainless Steel with Regard to the Influence of Heat Treatment. *Metals* **2018**, *8*, 220. [CrossRef]
28. Bachmann, F.; Hielscher, R.; Schaeben, H. Texture Analysis with MTEX—Free and Open Source Software Toolbox. *SSP* **2010**, *160*, 63–68. [CrossRef]
29. Murakami, Y. *Metal Fatigue*; Elsevier: Oxford, UK, 2019.
30. Engel, B.; Beck, T.; Moch, N.; Gottschalk, H.; Schmitz, S. Effect of local anisotropy on fatigue crack initiation in a coarse grained nickel-base superalloy. *MATEC Web Conf.* **2018**, *165*, 4004. [CrossRef]
31. Teklu, A.; Ledbetter, H.; Kim, S.; Boatner, L.A.; McGuire, M.; Keppens, V. Single-crystal elastic constants of Fe-15Ni-15Cr alloy. *Met. Mater. Trans. A* **2004**, *35*, 3149–3154. [CrossRef]
32. Krupp, U. *Fatigue Crack Propagation in Metals and Alloys*; John Wiley & Sons: Hoboken, NJ, USA, 2007. [CrossRef]